

FULL ARTICLE

Quantitative phase-filtered wavelength-modulated differential photoacoustic radar tumor hypoxia imaging toward early cancer detection

Edem Dovlo¹, Bahman Lashkari¹, Sung soo Sean Choi¹, Andreas Mandelis^{*,1}, Wei Shi², and Fei-Fei Liu²

¹ Center for Advanced Diffusion-Wave and Photoacoustic Technologies (CADIPT), Department of Mechanical and Industrial Engineering, University of Toronto, 5 King's College Road, Toronto, ON M5S 3G8, Canada

² Ontario Cancer Institute, Princess Margaret Hospital, 610 University Ave., Toronto, ON M5G 2M9, Canada

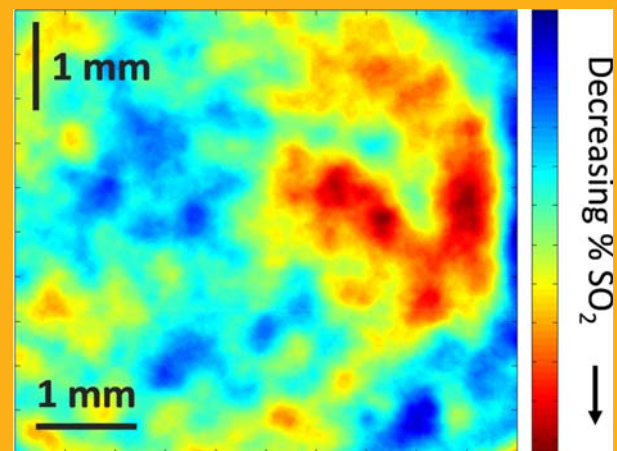
Received 2 June 2016, revised 21 August 2016, accepted 28 September 2016

Published online 20 October 2016

Key words: quantitative photoacoustic imaging, differential imaging, spectroscopy, tissue diagnostics, hypoxia, cancer diagnosis, frequency modulation

Overcoming the limitations of conventional linear spectroscopy used in multispectral photoacoustic imaging, wherein a linear relationship is assumed between the absorbed optical energy and the absorption spectra of the chromophore at a specific location, is crucial for obtaining accurate spatially-resolved quantitative functional information by exploiting known chromophore-specific spectral characteristics. This study introduces a non-invasive phase-filtered differential photoacoustic technique, wavelength-modulated differential photoacoustic radar (WM-DPAR) imaging that addresses this issue by eliminating the effect of the unknown wavelength-dependent fluence. It employs two laser wavelengths modulated out-of-phase to significantly suppress background absorption while amplifying the difference between the two photoacoustic signals. This facilitates pre-malignant tumor identification and hypoxia monitoring, as minute changes in total hemoglobin concentration and hemoglobin oxygenation are detectable. The system can be tuned for specific applications such as cancer screening and SO₂ quantification by regulating the amplitude ratio and phase shift of the signal. The WM-DPAR imaging of a head and neck carcinoma tumor grown in the thigh of a nude rat demonstrates the functional PA imaging of small animals *in vivo*. The PA appearance of the tumor in relation to tumor vascularity

is investigated by immunohistochemistry. Phase-filtered WM-DPAR imaging is also illustrated, maximizing quantitative SO₂ imaging fidelity of tissues.



Oxygenation levels within a tumor grown in the thigh of a nude rat using the two-wavelength phase-filtered differential PAR method.

* Corresponding author: e-mail: mandelis@mie.utoronto.ca, Phone: +1 416 978 5106, Fax: +1 416 978 5106

1. Introduction

A major advantage photoacoustics (PA) offers in preclinical/clinical applications is its intrinsically spectroscopic imaging capability [1–4] devoid of the depth limitations associated with optical methods. Properly chosen laser excitation wavelengths allow for selective enhancement of chromophore-specific contrast and spatial resolution. PA imaging is particularly sensitive to blood oxygenation, allowing for the potential measurement of critical diagnostic parameters for the metabolic state of lesions and therefore, early cancer diagnosis [5, 6].

In this work, we introduce wavelength-modulated differential photoacoustic radar (WM-DPAR) imaging for the functional imaging of a tumor *in vivo*. Laser beams at two distinct wavelengths are chirp-modulated out-of-phase ($\sim 180^\circ$ phase difference) with each other. The wavelengths are selected based on the absorption spectra of oxy- (HbO₂) and deoxy- (Hb) hemoglobin such that the molar extinction coefficients of oxy- and deoxy-hemoglobin coincide at one of the wavelengths (808 nm, near the isobestic point) while their molar extinction coefficients exhibit a significant difference at the other wavelength (i.e. 680 nm, in this case). This results in the PA signal being highly sensitive to changes in the optical parameters of blood at 680 nm while remaining relatively insensitive at 808 nm. The simultaneous use of the two wavelengths modulated out-of-phase significantly suppresses background noise by canceling out variations caused by the local fluence (capable of undermining spectral interpretation of PA images), while conversely amplifying the difference between the two signals, thus yielding high sensitivity and specificity for accurate tissue hypoxia assessment.

Tumor hypoxia has become a hallmark of cancer diagnostics and a critical issue in cancer therapy management [7–9]. Cancer is a major health problem worldwide and the second leading cause of death (one in four deaths) in the United States [10] alone. Early cancer detection and treatment significantly increase the chances of survival [11]. Hyperproliferating cancerous cells [12–14] resulting from genetic mutations drastically alter oxygen and nutrient utilization [15] such that characteristic metabolic changes are redirected to support the large biosynthetic demands of cell growth and proliferation. The result is the rapid development of a dense microvascular network via angiogenesis to perpetuate tumor growth during the multistage development of invasive cancers (pre-malignant and malignant phases alike) [16], and the fall in intratumoral oxygenation levels causing a hypoxic mass. Dilated and tortuous abnormal vessels form in the locally increased microvascular density region. PA imaging is investigated for microvessel quantitation as a prognostic param-

eter for head and neck squamous cell carcinoma as done in pathology by analyzing immunohistochemically (IHC) stained tissue specimens under a microscope [17–19]. Ultrasound (US), though useful in the diagnostic assessment largely for palpable mass analysis, distinguishing between solid masses and cysts, and guiding biopsies, is usually unable to evaluate early cancer, as it often shows no anatomical and morphological differences between the tumor and healthy tissue as yet and is operator-dependent. A comparison is made between US and PA images with histopathological corroboration.

Though several tumor hypoxia assessment modalities exist, none has been clinically approved for routine practice, thereby impeding the clinical development of hypoxia-based therapies. Polarographic electrodes, the current benchmark for tumor hypoxia detection and characterization [7], are highly invasive and require significant technical skill making measurement repeatability extremely challenging. The method also overestimates hypoxia in necrotic sample regions due to the inability of the probe to discriminate between viable and necrotic tissue [20]. Tumor hypoxia assessment is valuable to radiation oncologists, surgeons, and biotechnology and pharmaceutical companies engaged in the development of hypoxia-based therapies or treatment strategies [7, 11], ultimately improving patient outcomes.

Accurate noninvasive techniques for tumor hypoxia assessment and monitoring are needed in order to develop effective hypoxia modification therapies. Suited for *in vivo* clinical assessment of tumor hypoxia are noninvasive modalities that rely on endogenous markers, including near-infrared (NIR) spectroscopy/tomography [21, 22], blood oxygen level-dependent MRI (BOLD-MRI) [23] and photoacoustic tomography (PAT) [4, 24, 25]. NIR spectroscopy is limited in tissue penetration and low spatial resolution [26] whereas BOLD-MRI, though capable of providing useful complementary qualitative information, is deoxyhemoglobin concentration-dependent [27] (instead of pO₂ directly) making it susceptible to the influence of other independent variables not related to tissue oxygenation. Biomedical PAT detects less-scattering acoustic waves generated from absorbed electromagnetic energy with comparable axial resolution (\sim mm) and signal-to-noise ratio (SNR) facilitating accurate tumor hypoxia assessment [6]. The feasibility of the WM-DPAR imaging modality has been demonstrated using heparinized sheep blood at decreasing oxygenation levels circulating in plastic tubing [28]. The method was shown to be more sensitive to minute changes in SO₂ and tHb than single-wavelength FD-PAR imaging, with significant improvement in sensitivity, dynamic range (contrast), SNR and spatial resolution. In this paper, the WM-DPAR modality is further applied for accurate quantitative absolute SO₂ imaging *in vivo* and

monitoring of a rat in contrast with a two single-wavelength FD-PAR method. This is particularly valuable for clinical applications, as benchmarks of tumor formation such as angiogenesis and hypoxia can be detected.

The WM-DPAR imaging modality herein described operates on frequency domain (FD) principles using compact, inexpensive continuous-wave (CW) lasers, instead of the bulkier and expensive pulsed lasers used in conventional biomedical PA. The FD modality possesses depth-selective imaging capabilities [29] and applies matched filtering to generate a high peak power cross-correlation response. Furthermore, the WM-DPAR imager possesses higher diagnostic power and reliability at each probed subsurface depth as it provides three pairs of images (each pair being amplitude and phase-based) congruently instead of one in pulsed PA imaging. It provides separate images for the two applied wavelengths as well as the differential image. Since the phase tends to be more localized and of higher dynamic range (contrast) than amplitude as well as being optical fluence independent, it can be used to further improve the SNR and spatial resolution of images [30].

2. Theoretical background

A PA image is an estimate of the distribution of initial acoustic pressure arising from the optical absorption when tissue is irradiated with a light pulse which can be described as

$$p(x) = \Gamma(x) h(x) = \Gamma(x) \mu_a(x) \Phi(x, \mu_a, \mu_s, g) \quad (1)$$

where x is the spatial variable, Γ is the Grüneisen parameter of the tissue, μ_a, μ_s are the absorption and scattering coefficients, respectively, and Φ is the wavelength-dependent fluence distribution that depends on μ_a (and μ_s), resulting in the nonlinear dependence of the absorbed energy density, h , on chromophore concentrations.

The absorption coefficient of blood is dominated by the optical absorption of hemoglobin. It is thus represented as

$$\mu_a(\lambda, C_{\text{tHb}}, \text{SO}_2) = \ln(10) C_{\text{tHb}} [\text{SO}_2 \epsilon_{\text{HbO}_2, \lambda} + (1 - \text{SO}_2) \epsilon_{\text{Hb}, \lambda}] \quad (2)$$

where C_{tHb} is the total hemoglobin concentration (and therefore SO_2 can be defined as $\text{SO}_2 = C_{\text{HbO}_2} / C_{\text{tHb}}$), and $\epsilon_{\text{HbO}_2}, \epsilon_{\text{Hb}}$ are the molar extinction coefficients of oxy- and deoxy-hemoglobin at the specific wavelength, λ .

Using the quotient of two single-wavelength PAR amplitude measurements in the quantification of SO_2 , allows for the elimination of the effect of the variation in Γ between different tissue types, without assuming uniform Γ as commonly used throughout the tissue [31]. The quotient approach, herein referred to as the two single-wavelength PAR method, also eliminates the effect of the C_{tHb} (or hematocrit level) and system transfer function, by careful, painstaking pressure normalization using laser fluence from differing laser-dependent Gaussian-shaped beam profiles due to varying spot sizes required for adequate reliability. It is unlikely that the fluence distribution remains unchanged through a change in wavelength to an absorption peak as used in our methodology. The SO_2 expression is, therefore, obtained by

$$\frac{p_{680} / \Phi_{680}}{p_{808} / \Phi_{808}} = \frac{\mu_{a,680}}{\mu_{a,808}} = \frac{[\text{SO}_2 \epsilon_{\text{HbO}_2, 680} + (1 - \text{SO}_2) \epsilon_{\text{Hb}, 680}]}{[\text{SO}_2 \epsilon_{\text{HbO}_2, 808} + (1 - \text{SO}_2) \epsilon_{\text{Hb}, 808}]} \quad (3)$$

leading to

$$\text{SO}_2 = \frac{\epsilon_{\text{Hb}, 680} - \epsilon_{\text{Hb}, 808} R}{\alpha R - \gamma} \quad (4)$$

where

$$R = \frac{p_{680} / \Phi_{680}}{p_{808} / \Phi_{808}}; \quad \alpha = \epsilon_{\text{HbO}_2, 808} - \epsilon_{\text{Hb}, 808};$$

$$\gamma = \epsilon_{\text{HbO}_2, 680} - \epsilon_{\text{Hb}, 680}$$

Conversely, applying our two-wavelength differential PAR amplitude method using the WM-DPAR imager, the effect of the unknown wavelength-dependent fluence, which is a significant concern in conventional linear spectroscopy, can be eliminated using a ratio of two out-of-phase differential PAR measurements. This modality, however, depends on the local hematocrit level, unlike the two single-wavelength PAR amplitude mode. Slight measurement errors are introduced when the typical range of C_{tHb} from the literature (34–57% [32, 33]) for 13-week old female rats is considered, as used in our experiment. The differential PAR amplitude signal can be described using Eq. (1) as

$$p_{\text{diff}} \propto \mu_{a,680} - k \mu_{a,808} = \ln(10) C_{\text{tHb}} [\text{SO}_2 (\epsilon_{\text{HbO}_2, 680} - k \epsilon_{\text{HbO}_2, 808}) + (1 - \text{SO}_2) (\epsilon_{\text{Hb}, 680} - k \epsilon_{\text{Hb}, 808})] \quad (5)$$

where k is a system constant experimentally determined from the amplitude ratio (A_{680} / A_{808}) and phase difference ($\theta_{680} - \theta_{808}$) applied between the two laser wavelengths. This experimental determination is no easy feat without prior knowledge of the

$\mu_{a,680}$ and $\mu_{a,808}$ for a reference blood sample, which is often unknown or involves some invasive procedure. It is important to note here that k must also be carefully selected with respect to the specific chromophore characteristics (for example, HbO₂/Hb absorption spectra, in our case) for accurate results and data integrity. Processing the differential PAR signals relative to a reference differential PAR measurement, enables the determination of SO₂ devoid of the effects of the k determination and without another calibration (proportionality between differential PAR signal and k) in order to make use of a relative k instead. SO₂ is, thus, determined as

$$SO_2 = \frac{SO_2^{\text{ref}}(ap_{\text{diff}} + \beta \ln(10) C_{\text{tHb}}) + \epsilon_{\text{Hb},808}(p_{\text{diff}} - p_{\text{diff}}^{\text{ref}})}{ap_{\text{diff}}^{\text{ref}} + \beta \ln(10) C_{\text{tHb}}} \quad (6)$$

where

$$\beta = \epsilon_{\text{HbO}_2,680}\epsilon_{\text{Hb},808} - \epsilon_{\text{Hb},680}\epsilon_{\text{HbO}_2,808}$$

3. Materials and methods

3.1 Experimental set-up

Our system employs a 680 nm laser (LDX-3230-680; MO, USA) and a CW 808 nm laser diode (Jenoptik JOLD-120-QPXF-2P, Goeschwitz, Jena, Germany) for illumination. The 680 nm laser, with a maximum optical power (out-of-fiber) of ~1.4 W, is integrated with a customized laser driver (VFM5-25; MESSTEC, BY, DE) on an aluminum heat sink, while the 808 nm laser, with a maximum power of 5 W, is modulated using a software function generator. A frequency-sweep range of 300 kHz–3 MHz is applied to the lasers. A coupler is employed to better align both laser beams to the same spot and then a collimator (F230SMA-B; ThorLabs, NJ, USA) is used for collimating into a 0.8 mm diameter. A 3.5 MHz single-element ultrasonic transducer (C383; Olympus Panametrics, CA, USA) revolves around the sample to detect the generated PA signals. Most components of the set-up have freedom of motion in all directions (X , Y and Z). The sample and transducer are fully submerged in water for acoustic coupling. A pre-amplifier (5662; Olympus Panametrics, CA, USA) is used for PA signal amplification. The NI PXIe-1065 (National Instruments, Austin, TX, USA) data acquisition system collects the data needed for image reconstruction via signal processing using custom Lab View (National Instruments, Austin, TX, USA) and Matlab software code. The

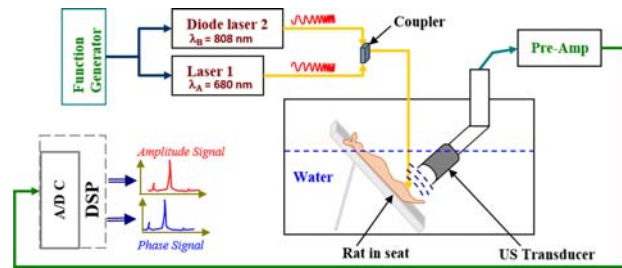


Figure 1 Block diagram of the experimental set-up of the WM-DPAR imaging system.

block diagram of the experimental set-up is shown in Figure 1.

3.2 Cancer cell preparation

Human hypopharyngeal head and neck squamous cell carcinoma FaDu cell lines were obtained from the American Type Culture Collection (Manassas, VA), and cultured in MEM F-15 supplemented with 10% fetal bovine serum. The right thigh of the nude rat was injected subcutaneously with 4.8×10^6 cultured cells/100 μ l and imaged consecutively over a three week period (results presented for one session). The animal was fully anesthetized throughout the experiment by administering 1.4 L/min of oxygen and 1 L/min of isoflurane gas. An IR lamp and a heater with a thermostat were used to regulate the animal body temperature. The experiment was performed under the guidelines of animal protocol 20011459 approved by the Division of Comparative Medicine (DCM) of the Faculty of Medicine, University of Toronto. Animal handling was also performed according to guidelines for laboratory animal care.

3.3 Imaging procedures

Detailed descriptions of the foundations of our WM-DPAR (and FD-PAR) technique are available elsewhere [4, 30, 34]. The superior accuracy of the WM-DPAR method in SO₂ quantification of an *in-vitro* blood-containing plastisol phantom over other PA modalities has also been shown in [35] and verified using a gas analyzer (gold standard). The sample (rat thigh) is positioned near the center of rotation, 25 mm from the surface of the transducer, and 100 chirps are coherently averaged to enhance the SNR of the PA signals. Moreover, to optimize the WM-DPAR method, the power of the two lasers is tuned to achieve a unity amplitude ratio (~240 mW/cm² power density over a 2 cm beam diameter, which is

within safe maximum permissible exposure (MPE) limits) and the phase difference to 180° so that the differential PA signal of HbO_2 is minimized (zeroed). The validity and sensitivity of the WM-DPAR modality is tested in comparison to single-wavelength FD-PAR tomography by imaging the subcutaneously cancer cell-injected right thigh of a nude rat. The morphological size of the tumor region of interest (ROI) is measured at the time of imaging to be ~ 12 mm (anterior-posterior) $\times 12$ mm (medial-lateral) $\times 3$ mm (height above skin) using a vernier caliper.

A horizontal field of view (FOV) of the ROI of 50 mm is achieved within a ~ 20 min measurement time. A relaxation time (in which the laser is off) of 55% of the imaging time is required for consecutive imaging. Parallel acquisition of detection elements was not possible in this version. Providing additional National Instruments (NI) cards and detection elements, simultaneous acquisition for data collection can improve the frame rate for real-time imaging (i.e. ~ 25 Hz). The system is also adequate for integration with clinical US systems for co-registration since a FD beamforming algorithm similar to that employed in conventional US imaging can be used for PA image reconstruction. The reconstructed image is the spatial cross-correlation function between the PA response and the reference signal used for laser source modulation (the radar principle).

4. Results and discussion

A photograph of the position of the rat placed in its seat, relative to the transducer, is provided in Figure 2(b). The post-surgery tissue specimen obtained for histopathology analysis measuring at 10 mm $\times 10$ mm $\times 4$ mm is also shown in Figure 2(a). The red circle marks the tumor ROI. The presence of a palpable mass is evident in a raised lump at the ROI thirteen days after injecting the cancer cells (at the time of imaging). The pure US image of the cancer cell-injected rat was obtained using the Sonix-TOUCH US imager at a frequency of 4 MHz as shown in Figure 2(c). The tumor, though not immediately obvious and distinguishable from other tissue such as muscle and tendon, can be seen as an unsharply delineated, irregular mass with inhomogeneous echo internal structure (indicated by the dashed white oval).

Histopathological studies and validation were conducted to confirm the presence of the cancerous tumor and its vascularity in the right thigh of the rat. Hematoxylin and eosin (H&E) staining and IHC staining were performed on the removed tissue and the stained sections were reviewed under a microscope with $\times 20$ magnification as shown in Figure 3.

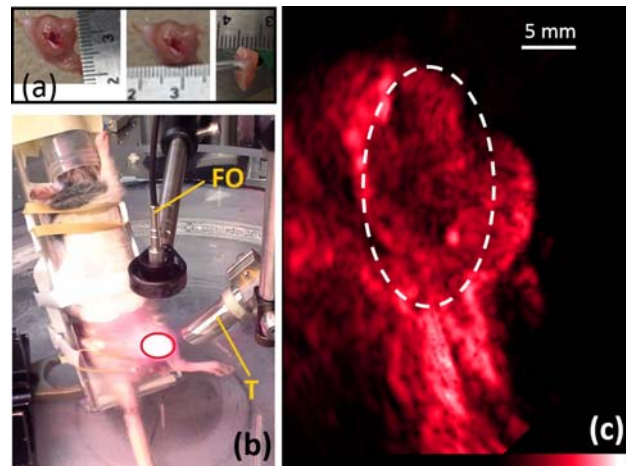


Figure 2 (a) Removed tumor showing its length, width and height; (b) Photograph of experimental set-up showing rat secured to the seat and the relative position of the irradiation source and transducer to it; (c) Pure US image obtained from commercial Ultrasonix imager FO: Optical fiber; T: Transducer.

A biomarker for blood vessel endothelium (CD31) is used on tissue specimens. H&E staining shows a cellular neoplasm arranged in nests and sheets (Figure 3(a)). The surrounding healthy tissue shows eosinophilic hyaline staining. Matching CD31 IHC staining reveals an increased overall spread of tumor blood microvessel density over the entire lesion as a result of the cancer (Figure 3(b)), appearing more pronounced at the lesion border than in certain areas. Areas with high vascularity are observed in the lesion periphery (Figure 3(c) – black border; (d) – green border) and those with mostly lower vascularity are in the center (Figure 3(e) – blue border; (f) – red border) of the lesion.

Although the location of the PA tomography FOV (perpendicular to the skin/tumor) does not provide composite 3D images for direct comparison with Figure 3 (tumor slices parallel to the skin used for H&E and IHC staining), the histopathological analysis corroborates the PAR imaging results, confirming (pre)malignancy and providing spatial features of the tumor (slice) useful as an image location reference.

The reconstructed PAR images in Figure 4 clearly indicate the location of part of the tumor and other relevant absorbing markers (like the skin, not included for clarity) from the transducer surface. The PA vertical FOV is through the center of the dashed oval shown in the US image (Figure 2(c)). The image maximum intensity corresponds to the maximum signal amplitude obtained for a given mode, indicating the presence of an absorber. The PAR images show a confined region of high intensity measuring ~ 3 mm (only part of the tumor due to illumination limitations). The PAR images, unlike

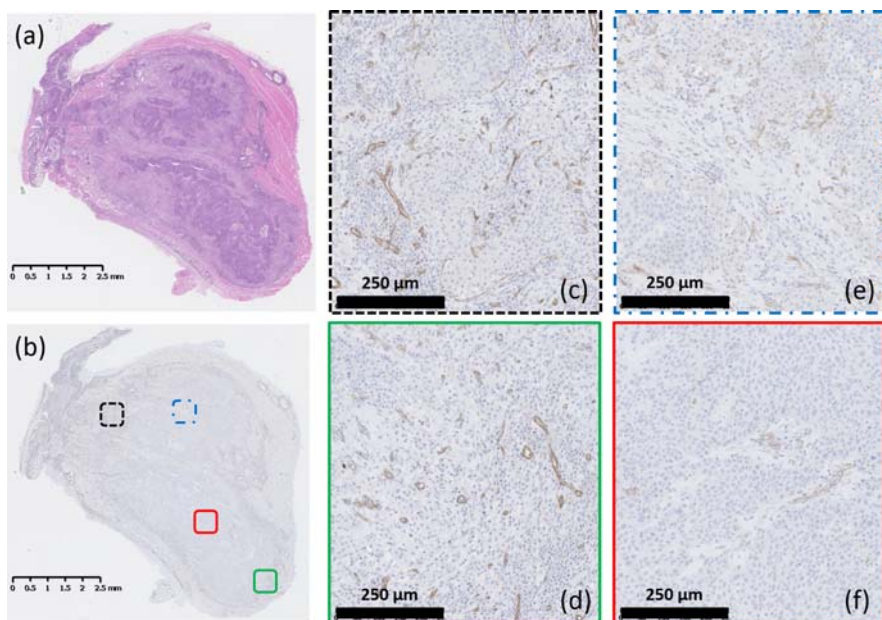


Figure 3 Post-surgical histopathological analysis via xenografts in which (a) the H&E stained tumor slide shows the cancer region, and (b) the CD31 stained slide shows an inhomogeneous vascular distribution as highlighted in the selected areas (c)–(f) at the tumor borders and center.

their US counterparts, are less sensitive to the presence of the surrounding tissue, but are highly sensitive to the presence of increased blood flow in the tumor. Thus, the PAR images exhibit better contrast and sensitivity, providing much clearer information regarding the tumor. This is particularly significant for much earlier stage tumor imaging: PAR images (not shown) reveal the tumor only six days after cancer-cell injection while the tumor is indistinguishable in the corresponding US image. Normalized amplitude-only and phase-only images are obtained for the single-wavelength 680 nm (Figure 4(a), (d)) and 808 nm (Figure 4(b), (e)) methods as well as the differential PAR modality (Figure 4(c), (f)) using the WM-DPAR system. Normalization is achieved by scaling each image to values within [0, 1] using the maximum intensity. A common maximum is applied

to the 680 nm and 808 nm images to facilitate adequate comparison and portrayal of the tumor. The 680 nm PAR amplitude image (Figure 4(a)) shows much higher intensity for Hb compared to HbO₂, while the 808 nm PAR amplitude image (Figure 4(b)) exhibits higher intensity for tHb in general. The differential PAR mode is tuned to zero local fluence-induced variations at the highest SO₂ level, in order to enhance sensitivity and specificity for accurate hypoxia monitoring. Differential PAR amplitude, therefore, increases with decreasing SO₂ with improved dynamic range. A relative intensity map of Hb and HbO₂ is obtained in Figure 4(c), though embedded in significant background intensities. This demonstrates the inability of the differential PAR amplitude to clearly differentiate the reduced relative intensity map of Hb and HbO₂ from the back-

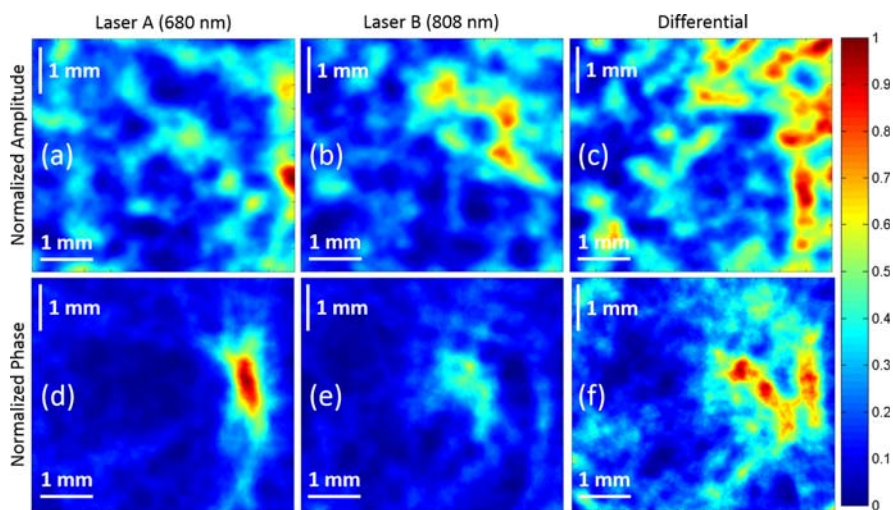
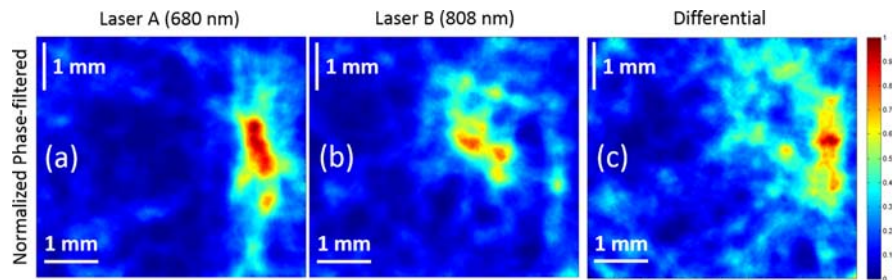


Figure 4 Normalized reconstructed PAR images using the 680 nm laser only (a, d), PAR images using the 808 nm laser only (b, e), and differential PAR images (c, f) using both lasers for *in vivo* imaging of a nude rat subcutaneously injected with cancer cells. Laser irradiation is from above at $\sim 45^\circ$ to the transducer (revolving counterclockwise over 180° from the bottom of the images).

Figure 5 Normalized reconstructed phase-filtered PAR images using (a) the 680 nm laser only, (b) the 808 nm laser only, and (c) the differential PAR modality using both lasers for *in vivo* imaging of a nude rat subcutaneously injected with cancer cells.



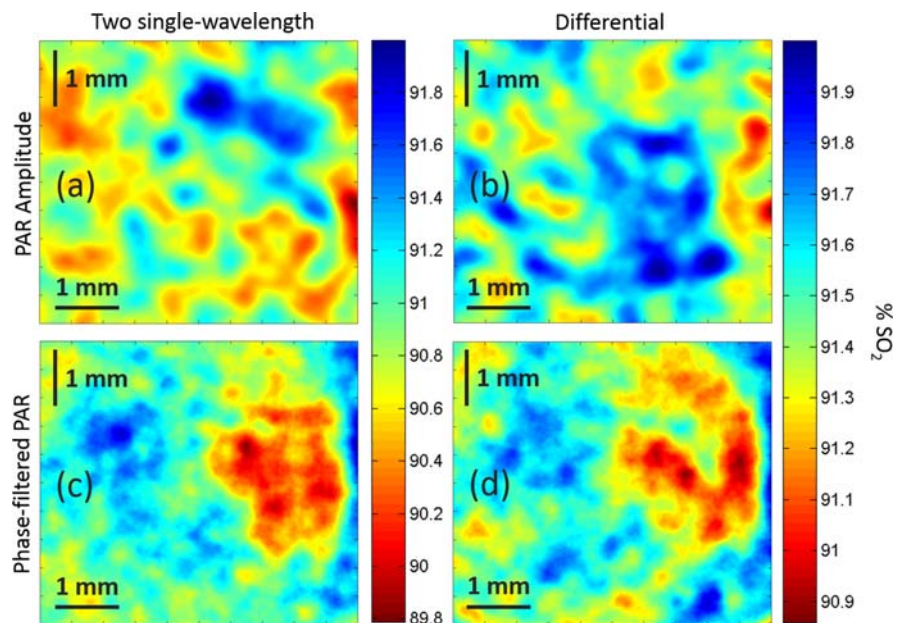
ground noise in a complex system, such as imaging *in vivo*. The phase images (Figure 4(d), (e), (f)) show a more localized tumor with better contrast and spatial location consistency than the amplitude images (Figure 4(a), (b), (c)).

Filtering the amplitude with the inverse of the standard deviation (SD) of the phase produces images with improved contrast and resolution. The tumor in the phase-filtered images shown in Figure 5 for the single-wavelength 680 nm, single-wavelength 808 nm and differential PAR modalities, respectively, seems just as localized and particularly more accentuated (higher contrast) due to the suppressed background absorption and noise resulting from phase-filtering. Coupled with the amplified signal difference between the out-of-phase modulated lasers used in the differential PAR modality, further enhancement in the sensitivity and dynamic range of the phase-filtered differential WM-DPAR image (Figure 5(c)) is observed. This results in higher fidelity in size and shape reconstruction, which enables more accurate PA visualizations to be generated. Hence, the phase-filtered WM-DPAR image provides more highly resolved, better contrast and dimension-consistent images of

the tumor compared to the single-wavelength 680 nm and 808 nm FD-PAR modes separately.

Figure 6 shows the quantitative SO_2 images obtained using the two single-wavelength FD-PAR method (Figure 6(a), (c)) compared to the WM-DPAR modality (Figure 6(b), (d)). A baseline SO_2 level of 92% is applied for HbO_2 with the typical SO_2 range in healthy rats being 89–92% [36–38]. From the quantitative imaging results of the imaged FOV calculated using Eq. (6) with $C_{\text{tHb}} = 44\%$, the tumor shows lower SO_2 levels than the surrounding tissue in the differential PAR amplitude case (Figure 6(b)), though not falling below the nominally normal SO_2 range. Applying Eq. (4), the two single-wavelength FD-PAR amplitude mode (Figure 6(a)) overestimates the hypoxic level with depth, as can be deduced by inspection of the PAR amplitude images in Figure 4(a), (b), (c). This is due to the effect of variations in surface absorption between the different wavelengths, and consequently, the significant variations in fluence with depth. Simultaneous detection and acquisition would be a useful improvement to better and more adequately interrogate and observe the entire ROI instead of a single scanline.

Figure 6 Oxygenation levels within the tumor using (a) two single-wavelength PAR amplitude measurements, (b) two-wavelength differential PAR amplitude method, (c) two single-wavelength phase-filtered PAR measurements, and (d) two-wavelength phase-filtered differential PAR method.



Upon filtering the quantitative SO₂ two single-wavelength and two-wavelength differential PAR amplitude images with the inverse of the SD of the phase from the combined 808 nm and 680 nm, and differential PAR measurements, respectively, the results are significantly improved with better correlation to the qualitative phase-filtered PAR images. A combination of the inverse of the SD of the phase from the 808 nm and 680 nm modes is employed, instead of that of the 808 nm measurement only, to allow for dimensional integrity of the tumor. The two single-wavelength phase-filtered SO₂ PAR image (Figure 6(c)) is, therefore, greatly improved with better spatial consistency of the tumor compared to the single-wavelength phase-filtered 680 nm and 808 nm FD-PAR modes separately. Furthermore, the two-wavelength phase-filtered differential SO₂ PAR image (Figure 6(d)) shows significantly improved sensitivity with adequate size and shape fidelity for accurate quantitative SO₂ visualization.

The experimental results obtained show that single-wavelength PAR images may be qualitatively incomplete and quantitatively unreliable, whereas differential PAR modality can provide the most reliable and quantitatively accurate images.

5. Conclusion

The imaging of cancer cells injected into the right thigh of a nude rat demonstrated the validity of phase-filtered WM-DPAR modality for the functional imaging of small animals *in vivo*. Experimental results presented demonstrate live animal testing and show enhancements in SNR, contrast and spatial resolution, providing clearer information regarding the tumor via phase-filtered differential PA imaging owing to the high localization of the phase, minimization of background noise and amplification of signal differences.

The WM-DPAR modality was also used in the quantification of SO₂, showing greater sensitivity to minute changes in tHb and SO₂, than single-wavelength FD-PAR imaging. This is valuable for clinical applications, as benchmarks of tumor formation such as angiogenesis and hypoxia, can be detected. The WM-DPAR images were further improved in terms of dimensional integrity, dynamic range (contrast), SNR, and spatial resolution by applying image normalization techniques and phase-filtering. Potential problems (less quantitative reliability) with consecutive single-wavelength imaging contrast widely used in multispectral PA imaging were revealed and a method for quantitative differential PA imaging that yields precise contrast based on the level of tumor hypoxia was presented. Further studies are underway to extend the WM-DPAR modality to three-di-

mensional quantitative tumor hypoxia imaging and fully amalgamate both US and WM-DPAR modalities into a single imager.

Acknowledgements A. Mandelis is grateful to the Natural Sciences and Engineering Research Council of Canada (NSERC) for a Discovery Grant; to NSERC and CIHR for a CHRP grant; and to the Canada Research Chairs (CRC) Program.

Author biographies Please see Supporting Information online.

References

- [1] J.-T. Oh, M.-L. Li, H. F. Zhang, K. Maslov, G. Stoica, and L. V Wang, *J. Biomed. Opt.* **11**(3), 34032 (2006).
- [2] D. Razansky, M. Distel, C. Vinegoni, R. Ma, N. Perrimon, R. W. Köster, and V. Ntziachristos, *Nat. Photonics* **3**(7), 412–417 (2009).
- [3] S. Telenkov and A. Mandelis, *Rev. Sci. Instrum.* **81**(12), 124901 (2010).
- [4] B. Lashkari, S. soo Choi, E. Dovlo, S. Dhody, and A. Mandelis, *IEEE J. Sel. Top. Quantum Electron.* **22**(3), 127–136 (2016).
- [5] S. Mallidi, G. P. Luke, and S. Emelianov, *Trends Biotechnol.* **29**(5), 213–221 (2011).
- [6] L. V. Wang and H. Wu, *Biomedical Optics: Principles and Imaging*. (John Wiley & Sons, 2012).
- [7] J. C. Walsh, A. Lebedev, E. Aten, K. Madsen, L. Marciano, and H. C. Kolb, *Antioxid. Redox Signal.* **21**(10), 1516–1554 (2014).
- [8] R. A. Gatenby and R. J. Gillies, *Nat. Rev. Cancer* **4**(11), 891–899 (2004).
- [9] P. P. Hsu and D. M. Sabatini, *Cell* **134**(5), 703–707 (2008).
- [10] R. Siegel, J. Ma, Z. Zou, and A. Jemal, *CA. Cancer J. Clin.* **64**(1), 9–29 (2014).
- [11] M. Xu and L. V Wang, *Rev. Sci. Instrum.* **77**(4), 041101 (2006).
- [12] American Cancer Society, *Oncogenes, tumor suppressor genes and Cancer*, 2014.
- [13] J. S. Bertram, *Mol. Aspects Med.* **21**(6), 167–223 (2000).
- [14] D. Hanahan and R. A. Weinberg, *Cell* **100**(1), 57–70 (2000).
- [15] P. Vaupel, F. Kallinowski, and P. Okunieff, *Cancer Res.* **49**(23), 6449–6565 (1989).
- [16] D. Hanahan and R. A. Weinberg, *Cell* **144**(5), 646–674 (2011).
- [17] N. Weidner, *Am. J. Pathol.* **147**(1), 9–19 (1995).
- [18] L. Hlatky, P. Hahnfeldt, and J. Folkman, *J. Natl. Cancer Inst.* **94**(12), 883–893 (2002).
- [19] M. Heijblom, D. Piras, M. Brinkhuis, J. C. G. van Hesp, F. M. van den Engh, M. van der Schaaf, J. M. Klaase, T. G. van Leeuwen, W. Steenbergen, and S. Manohar, *Sci. Rep.* **5**, 11778 (2015).
- [20] P. Vaupel, M. Höckel, and A. Mayer, *Antioxid. Redox Signal.* **9**(8), 1221–1235 (2007).

- [21] R. Boushel, H. Langberg, J. Olesen, J. Gonzales-Alonzo, J. Bülow, and M. Kjaer, *Scand. J. Med. Sci. Sports* **11** (4), 213–222 (2001).
- [22] G. Casey, *Nurs. Stand.* **15**(47), 46–53; quiz 54–55 (2001).
- [23] S. Chopra, W. D. Foltz, M. F. Milosevic, A. Toi, R. G. Bristow, C. Ménard, and M. A. Haider, *Int. J. Radiat. Biol.* **85**(9), 805–813 (2009).
- [24] K. M. Stantz, B. Liu, M. Cao, D. Reinecke, K. Miller, and R. Kruger, *Biomedical Optics* **2006**, 608605–608612 (2006).
- [25] M.-L. Li, J.-T. Oh, X. Xie, G. Ku, W. Wang, C. Li, G. Lungu, G. Stoica, and L. V. Wang, *Proc. IEEE* **96**(3), 481–489 (2008).
- [26] M. Wolf, M. Ferrari, and V. Quaresima, *J. Biomed. Opt.* **12**(6), 062104 (2007).
- [27] S. P. Li, A. R. Padhani, and A. Makris, *J. Natl. Cancer Inst. Monogr.* **2011**(43), 103–107 (2011).
- [28] E. Dovlo, B. Lashkari, S. soo S. Choi, and A. Mandelis, in *SPIE BiOS*, p. 97081Y, International Society for Optics and Photonics (2016).
- [29] S. Telenkov and A. Mandelis, *J. Biomed. Opt.* **11**(4), 044006 (2006).
- [30] E. Dovlo, B. Lashkari, A. Mandelis, W. Shi, and F.-F. Liu, *Biomed. Opt. Express* **6**(3), 1003–1009 (2015).
- [31] B. T. Cox, J. G. Laufer, and P. C. Beard, in *SPIE BiOS Biomed. Opt.*, p. 717713, International Society for Optics and Photonics (2009).
- [32] P. L. Lang, *Hematology Parameters for the Crl: CD[®]BR Rat*, 1993.
- [33] R. J. Probst, J. M. Lim, D. N. Bird, G. L. Pole, A. K. Sato, and J. R. Claybaugh, *J. Am. Assoc. Lab. Anim. Sci.* **45**(2), 49–52 (2006).
- [34] S. Choi, A. Mandelis, X. Guo, B. Lashkari, S. Kellnberger, and V. Ntziachristos, *Int. J. Thermophys.* **36**(5–6), 1305–1311 (2014).
- [35] S. S. S. Choi, B. Lashkari, E. Dovlo, and A. Mandelis, *Biomed. Opt. Express* **7**(7), 2586 (2016).
- [36] L. H. Gray and J. M. Steadman, *J. Physiol.* **175**, 161–171 (1964).
- [37] E. Klemetti, S. Rico-Vargas, and P. Mojon, *Lab. Anim.* **39**(1), 116–121 (2005).
- [38] E. Diederich, *Cardiovasc. Res.* **56**(3), 479–486 (2002).